Plasmonic Photoelectrochemistry: In View of Hot Carriers

Yuchao Zhang, Wenxiao Guo, Yunlu Zhang, and Wei David Wei*

Utilizing plasmon-generated hot carriers to drive chemical reactions has emerged as a popular topic in solar photocatalysis. However, a complete description of the underlying mechanism of hot-carrier transfer in photochemical processes remains elusive, particularly for those involving hot holes. Photoelectrochemistry enables to localize hot holes on photoanodes and hot electrons on photocathodes and thus offers an approach to separately explore the hole-transfer dynamics and electron-transfer dynamics. This review summarizes a comprehensive understanding of both hot-hole and hot-electron transfers from photoelectrochemical studies on plasmonic electrodes. Additionally, working principles and applications of spectroelectrochemistry are discussed for plasmonic materials. It is concluded that photoelectrochemistry provides a powerful toolbox to gain mechanistic insights into plasmonic photocatalysis.
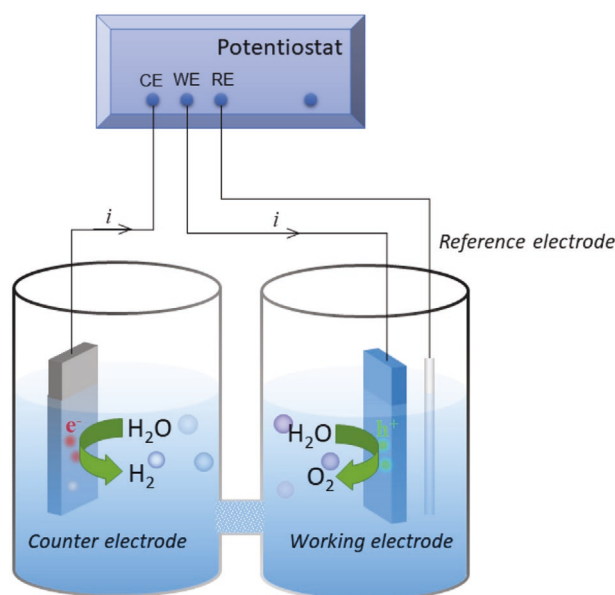
1. Introduction

Plasmonic metal (e.g., Au, Ag and Cu) nanoparticles (NPs) have attracted heightened interest in solar energy conversion, owing to their surface plasmon resonance (SPR) property.[1] As photocatalysts, they can efficiently utilize solar energy and drive photochemical reactions.[1–2] It is commonly accepted that the plasmonic enhancement takes effects via three pathways, i.e., hot carrier (electron-hole pairs), electromagnetic-field enhancement, and photothermal effect.[2a,b,3] As most photochemical reactions studied in photocatalysis are redox reactions, charge transfer must be present. Hence, hot carriers should play the major role in driving photochemical redox reactions. On the other hand, temperature can also influence redox reactions according to Nernst equation. Although not taken as the main component, photothermal effect should also be carefully considered in plasmon-driven photochemical reactions. The electromagnetic-field enhancement effect has been widely explored in the surface-enhanced Raman scattering (SERS) studies and comprehensive reviews have been published elsewhere.[3c,d] Hence, in this review, the effect of electromagnetic-field enhancement is not discussed.

Prof. Y.-C. Zhang,[+] W.-X. Guo, Dr. Y.-L. Zhang, Prof. W.-D. Wei
Department of Chemistry and Center for Catalysis
University of Florida
Gainesville, FL 32611, USA
E-mail: wei@chem.ufl.edu

The ORCID identification number(s) for the author(s) of this article can be found under https://doi.org/10.1002/adma.202006654.

[+]Present address: Key Laboratory of Photochemistry, CAS Research/Education Center for Excellence in Molecular Sciences, Institute of Chemistry, Chinese Academy of Sciences, Beijing 100190, P. R. China
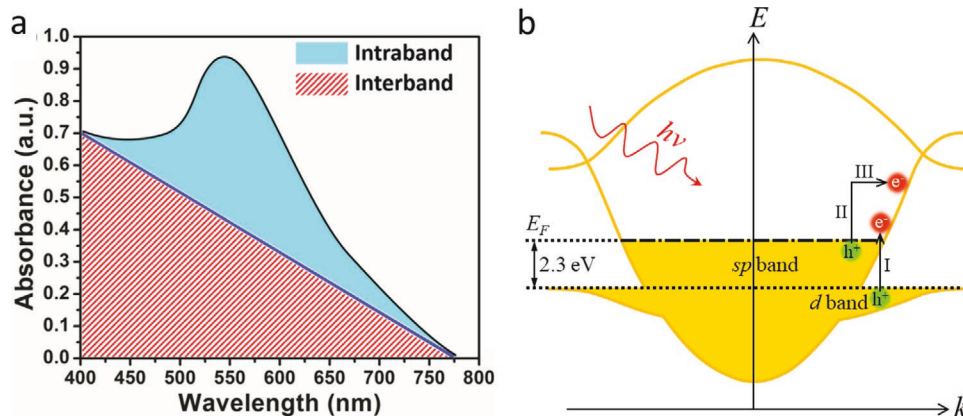
The physical understanding of plasmon-mediated hot-carrier generation can be found in our previous review.[1] For hot-carrier-induced photochemical reactions, mismatch between short lifetimes of hot carriers ($\approx$fs–ns)[2a–c] and long timescales of chemical reactions ($\approx$ms–s)[4] leads to low photocatalytic activities on plasmonic photocatalysts.[1,2d] The strategy of plasmon-mediated electron-transfer (PMET) on metal/semiconductor heterostructures was developed to overcome this incongruity.[2b,3b,5] Hot electrons generated on metal surfaces with sufficient energy can transfer across the Schottky barrier at metal/semiconductor interfaces and then be trapped at the conduction band (CB) of semiconductors. This strategy effectively prolongs lifetimes of hot electrons, which enables various reduction reactions.[5a,6] On the other hand, strategies for hot-hole manipulation are fewer than that of hot electrons.[2d,7] The faster relaxation dynamics and lower mobility of hot holes make them harder to be trapped and stabilized when compared with hot electrons.[2d,8]

Photoelectrochemistry uses an electric field to force the separation of hot electrons and holes, which prolong lifetimes of hot carriers (**Figure 1**).[9] Moreover, photoelectrochemistry offers the convenience for exploring hole-transfer and electron-transfer dynamics separately by localizing hot holes on photoanodes and hot electrons on photocathodes (Figure 1). More importantly, photoelectrochemical (PEC) results (e.g., onset potential and photocurrent action spectrum) are also useful for revealing physical locations of active sites and energetics of hot carriers in plasmonic photocatalysis, which are usually the main focus of PEC studies.[10]

Identifying physical locations of active sites on plasmonic photocatalysts is important.[7,11] Taking plasmonic Au/TiO$_2$ heterostructures as an example, it was commonly believed that active sites for hot-electron-induced reactions were on TiO$_2$ surfaces and active sites for hot-hole-driven reactions were on Au surfaces.[11a,b,12] However, recent studies suggested that active sites for hot-hole-driven reactions were at Au/TiO$_2$ interfaces.[2d,7,11c] Such a discrepancy calls for more in-depth mechanistic studies to verify physical locations of those active sites.

Investigation of energetics of plasmon-generated hot carriers is another important but difficult topic due to the complicated electronic structures of plasmonic metals. For instance, on Au NPs, SPR absorption that generates hot carriers via intraband transition overlaps with the range of interband transition (**Figure 2**a, and an increasing portion of interband transition occurs at a shorter wavelength (Figure 2a).[13,14] Interband transition produces more-energetic d-band holes while intraband transition generates more-energetic sp-band electrons (Figure 2b).[13a,15] This special nature of plasmonic

Figure 1. A typical three-electrode PEC configuration. Here, using water splitting as an example, water oxidation occurs on the working electrode and water reduction occurs on the counter electrode.

photocatalysis distinguishes it from semiconductor photocatalysis, in which only interband transition exists. The multiple sources of hot carriers make the design and optimization of plasmonic photocatalysts rather complicated.
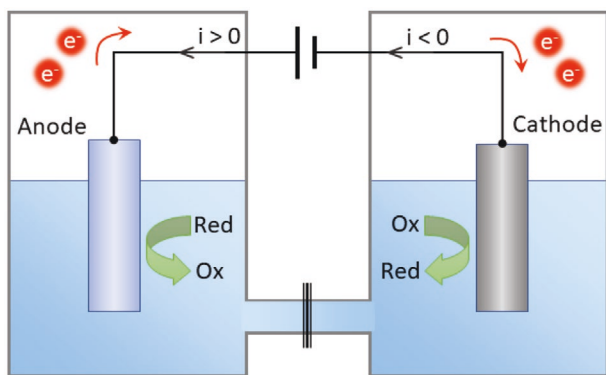
Furthermore, it is noteworthy that the resolution of electrochemical measurements is in the range of ≈ms – s.[16] In such timescales, hot carriers should relax to the Fermi level before they are detected. Therefore, the energetics of hot carriers revealed by PEC measurements are absolutely different from those studied by ultrafast spectroscopies (in the range of ≈fs – ns) that reported energies of around 1 eV for hot carriers.[6,17] However, those widely-concerned photochemical reactions (e.g., water oxidation, CO_2 reduction) exhibit timescales longer than ≈ms.[1,2d,18] Hence, PEC tools should be the appropriate method for studying those reactions.

In semiconductor photocatalysis, photoelectrochemistry has demonstrated its strong capability in revealing physical locations of active sites and energetics of hot carriers.[18a,19] However, in the scope of plasmonic photocatalysis, PEC research remains underdevelopment. Particularly, distinct contributions of hot holes and hot electrons in various PEC behaviors are not clearly distinguished and verified, which hinders mechanistic understanding on physical locations of active sites and energetics of hot carriers. For instance, in a PEC water-splitting device using a Au/TiO_2 photoanode as the working electrode, hot-hole-driven water oxidation is the rate-determining step (RDS), rather than hot-electron-driven water reduction on the cathode. However, researchers mostly focused on the efficiency of hot-electron transfer across Au/TiO_2 interfaces rather than energetics of hot holes and dynamics of hot-hole transfer.[5b,10b,c,f] Hot-hole transfer at various interfaces (e.g., metal/semiconductor interfaces, electrode/electrolyte interfaces) needs to be re-considered to fully understand PEC behaviors of plasmonic electrodes. Furthermore, it is important to point out that PEC concepts and mechanisms developed for semiconductor photocatalysis cannot be directly transplanted into plasmonic photocatalysis. The definitions and physical meanings of PEC concepts (e.g., onset potential and open-circuit photovoltage (V_{ph})) need to be clarified in the plasmonic field.

Herein, we provide an overview of PEC approaches for mechanistic studies of plasmonic photocatalysis. Structures and working principles of photoanodes (metal or metal/n-type semiconductor) and photocathodes (metal/p-type semiconductor) are first clarified in Sections 2.1 and 2.2, respectively. Open-circuit potential (OCP) studies are summarized in Sections 3.1 to clarify distinct mechanisms of hot-electron and hot-hole transfer in various setups. Operating under closed-circuit conditions, linear sweep voltammetry (LSV, Section 3.2.1 and electrochemical impedance spectroscopy (EIS, Section 3.2.2 are discussed for identifying physical locations of active sites on plasmonic electrodes, while monochromatic incident photon-to-electron conversion efficiency (IPCE) measurements are discussed in Section 3.2.3 for distinguishing intraband and interband-excited hot carriers in driving photochemical reactions. Furthermore, combined with spectroscopies, spectroelectrochemical (SEC) measurements are summarized in Section 3.3 for uncovering more mechanistic information about plasmonic photocatalysis.

Figure 2. Interband transition and intraband transition. a) A schematic absorption spectrum of Au NPs, which consists of absorption from both intraband and interband transitions. b) The schematic of I) interband transition and II) intraband transition on a Au NP. III) Here, intraband transition is assisted by a phonon for momentum conservation. (a) Reproduced with permission.[14] Copyright 2015, AIP Publishing LLC.

**ADVANCED
SCIENCE NEWS**

www.advancedsciencenews.com

**ADVANCED
MATERIALS**

www.advmat.de

Figure 3. The schematic of an anode and a cathode. Oxidation reactions occur on an anode and reduction reactions occur on a cathode. Anodic current is defined as positive while cathodic current is negative.

## 2. Configurations of Plasmonic Photoelectrodes

In a general electrochemical setup, electrodes are classified as anodes (oxidation reactions) and cathodes (reduction reactions) (**Figure 3**), which are also applicable for plasmonic photoelectrodes. Structures and working principles of photoanodes (metal NP or metal/n-type semiconductor) and photocathodes (metal/p-type semiconductor) are clarified in Sections 2.1 and 2.2, respectively.

2.1. Photoanodes

Metal/n-type semiconductor heterostructures are extensively explored as photoanodes in plasmonic photocatalysis. [2b,3a,b,5b,g,10f,g,20] For n-type semiconductors, Fermi levels are located near CB. Upon contact with metals, semiconductors donate electrons to metals to equilibrate Fermi levels. This alignment generates an upward band bending at metal/semiconductor interfaces (termed as the "Schottky barrier").[1] Plasmon-generated hot electrons with sufficient energy can overcome the Schottky barrier and reach CB of semiconductors; then they are quickly swept away from interfaces due to the upward band bending (**Figure 4**a).[2a,b,5d] Those electrons then travel along the external circuit and are eventually accumulated at the counter electrode to participate in reduction reactions (e.g., water reduction, Figure 4a. Meanwhile, hot holes are left on metals to drive oxidation reactions (e.g., water oxidation, Figure 4a.[10f] As a result, an anodic photocurrent is observed on the working electrode. It is noteworthy that in this scenario, electron transfer is controlled by the potentiostat and reduction reactions at the counter electrode are not RDS. Instead, kinetics of hot-hole-driven photochemical reactions on the working electrode control the magnitude of photocurrent. For instance, when PEC water oxidation is performed on photoanodes, the large timescale mismatch between the slow kinetics of water oxidation and the short lifetimes of hot holes leads to a low anodic photocurrent.[4c–g,21] Moskovits and co-workers deposited
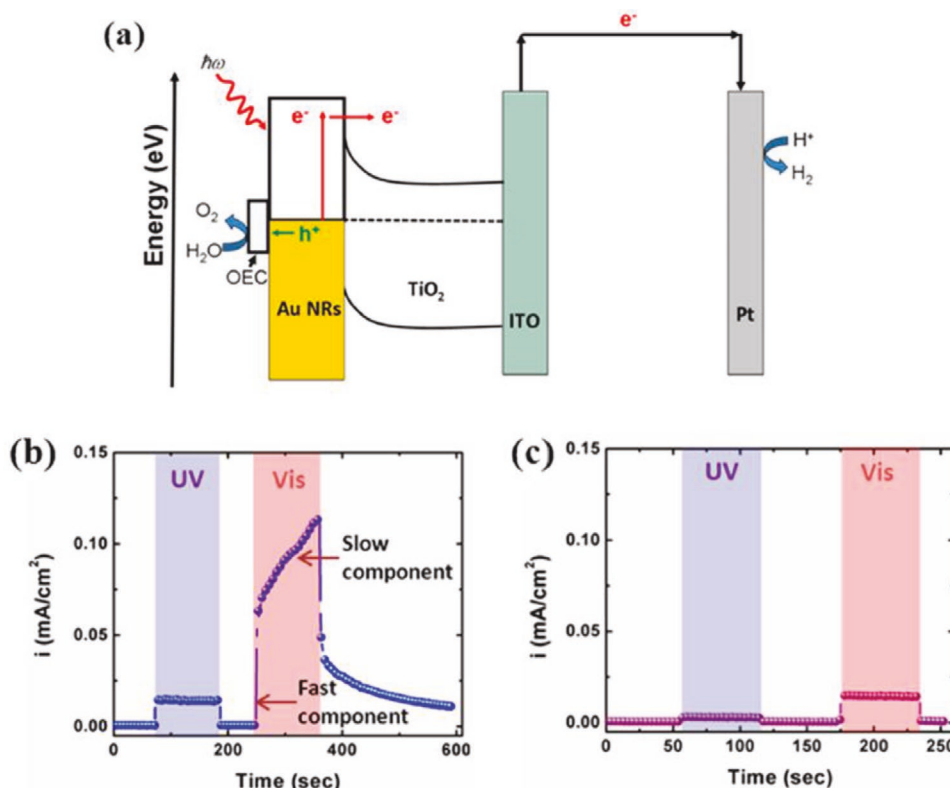
Figure 4. PEC water oxidation on a plasmonic metal/n-type semiconductor photoanode. a) Energy band diagram of a Au/TiO₂ photoanode. Under visible-light excitation, electron-hole pairs are generated on Au. Hot electrons are injected into TiO₂, and hot holes are extracted by Co-OEC for facilitating water oxidation. Photocurrent versus time plots for b) Au/TiO₂ with and c) without Co-OEC under UV and visible-light irradiation at 1 V$_{RHE}$. Reproduced with permission.[10f] Copyright 2012, American Chemical Society.
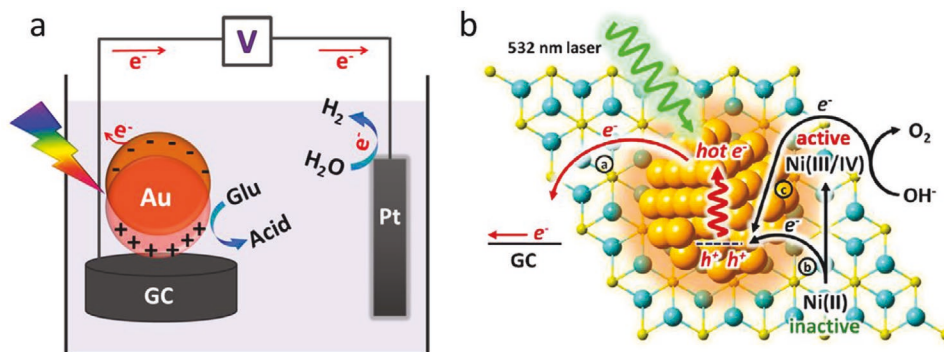
Figure 5. Plasmonic metal photoanodes. a) A PEC setup of plasmon-accelerated electrochemical oxidation of glucose. b) Scheme of charge transfer on a $Ni(OH)_2$/Au electrode. The dashed line indicates the Fermi level of Au NP. Light yellow, cyan, and orange spheres correspond to O, Ni, and Au atoms, respectively. (a) Reproduced with permission.[22a] Copyright 2017, American Chemical Society. (b) Reproduced with permission.[22c] Copyright 2016, American Chemical Society.

Co-based oxygen evolution catalyst (Co-OEC) on Au to trap hot holes in order to elongate their lifetimes and further catalyze water oxidation.[10f,g] As a result, a significantly enhanced anodic photocurrent was observed under visible-light illumination (Figure 4b,c). This phenomenon supports that dynamics of hot-hole transfer and kinetics of hot-hole-induced oxidation reactions are rate-determining factors that control photoactivity of metal/n-type semiconductor photoanodes.

Recently, metal NP electrodes without semiconductor substrates have also been reported to work as photoanodes.[22] It is believed that the Schottky barrier at metal/semiconductor interfaces limits collection efficiency of hot electrons, and the lower collection efficiency of hot electrons would lead to more electron-hole recombination on metal. Hence, metal NP electrodes without semiconductors are more promising for maximum utilization of hot carriers to drive chemical reactions directly on metal surfaces.[22a] Anodic photocurrents were observed on metal NP electrodes when plasmon-generated hot holes were efficiently captured by organic compounds (e.g., glucose[22a]

and methanol,[22b] **Figure 5**a or trapped by OER catalysts (e.g., $Ni(OH)_2$,[22c] Figure 5b. This area has just emerged, and so far, only Au was used for photoanode due to its relatively high stability among plasmonic metals.

2.2. Photocathodes

There are fewer reports on using plasmonic photocatalysts as photocathodes when compared with that of photoanodes. Photocathodes consist of metal/p-type semiconductor heterostructures, on which plasmon-generated hot holes are captured by p-type semiconductors and electrons are confined within metal NPs for driving reduction reactions (**Figure 6**a).[23] Efficiently collecting hot holes by semiconductors is the primary requirement for a highly active photocathode. Theoretically, holes generated by photo-excitation above interband threshold are significantly hotter than the corresponding electrons, which implies a greater collecting efficiency of hot holes than hot
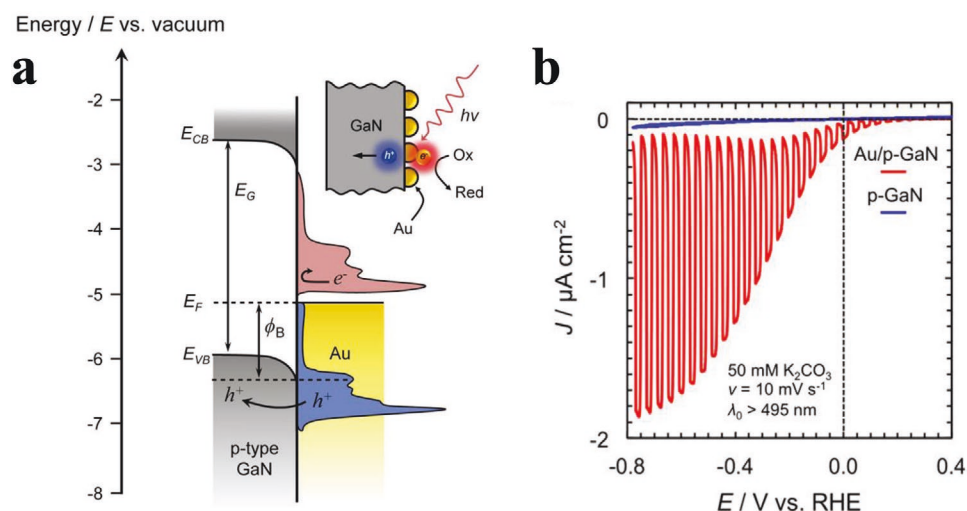
Figure 6. A plasmonic metal/semiconductor photocathode. a) Energy band diagram of Au/p-GaN photocathode, depicting E_{VB}, E_{CB}, E_G, E_F, and Φ_B. Plasmon excitation generated hot electrons (red) and hot holes (blue) above and below E_F of Au, respectively. Only those hot holes with energies larger than Φ_B was able to surmount interfacial barrier and populate available VB levels of p-GaN. b) LSV of Au/p-GaN (red) and bare p-GaN (blue) photocathodes. Reproduced with permission.[23a] Copyright 2018, American Chemical Society.

**ADVANCED
SCIENCE NEWS**

www.advancedsciencenews.com

**ADVANCED
MATERIALS**

www.advmat.de

electrons for a comparable Schottky barrier height (Φ_B) in this optical range.[23a,24] However, due to the relatively short mean-free path of hot holes ($\approx$5–10 nm)[23a,24] as well as the lack of suitable wide-band-gap p-type semiconductors, harvesting hot holes from plasmonic metals remains challenging. Recently, p-type gallium nitride (p-GaN) was employed as a semiconductor support in plasmonic photocathodes (Figure 6a).[23a] In Au/p-GaN heterostructures, Au NPs injected hot holes into the valence band (VB) of p-GaN and the adaptive Schottky barrier ($\Phi_B = 1.1$ eV) prevented holes from retrieving to Au.[23a] Hot electrons that were confined on Au contributed to the cathodic photocurrent in plasmon-driven CO_2 reduction (Figure 6b).[23a]

Photocathodes consist of nanostructured metal (Au and Ag) have also been recently reported for catalyzing reduction reactions (e.g., hydrogen evolution reaction, CO_2 reduction, and NO_3^- reduction reactions).[22b,25] Without the above-mentioned p-type semiconductor as a hole-trapping mediator, the electron-hole separation on the pure metal NP electrodes remains a big issue. It is noted that most previously reported photocurrent response on metal NP photocathodes was still low even under an intensive illumination.[22b,25] Surface modification with molecular electron/hole trapping mediators should be developed to achieve a decent charge separation for efficiently driving photochemical reactions.

Plasmon-driven hydrogen evolution reaction and CO_2 reduction have been hot topics but reports on plasmon-driven PEC N_2 fixation are still rare. Indeed, the redox potential of N_2 reduction is very negative (–4.16 V vs NHE),[26] which is beyond the energy level of plasmon-excited hot electrons. Even though the applied bias can lift up the Fermi level of photocathodes, it can be speculated that a very high overpotential need to be applied, which hinders its wide applications. However, several recent photocatalytic systems succeeded in achieving plasmon-driven N_2 fixation via surface engineering[27] and fabricating Au-Ru core-antenna nanostructures,[28] which effectively activated N_2 molecules and thus largely reduced the activation energy. Those strategies are promising to be applied when fabricating plasmonic photocathodes for driving PEC N_2 fixation.

3. Working Principles of Plasmonic PEC Measurements

PEC measurements are classified as open-circuit and closed-circuit tests. Different operating conditions (without or with applied bias) determine their distinct working principles. Herein, learning from semiconductor photoelectrochemistry, we clarify the working principles of PEC measurements on plasmonic electrodes in order to identify active sites for plasmon-driven chemical reactions and meanwhile estimate relevant energetics of hot carriers.

3.1. Open-Circuit Measurements

Under open-circuit conditions, no current flows through the electric circuit. Both plasmon-generated electrons and holes remain on working electrodes. Composition of electrolytes (e.g., a particular charge carrier scavenger) and surface property

of electrodes (e.g., surfactant modification, defect states, etc.) control the type of hot carriers (electrons or holes) that are preferentially accumulated on electrode surfaces, which determines the photoresponse of OCP (i.e., photovoltage, V_{ph}).
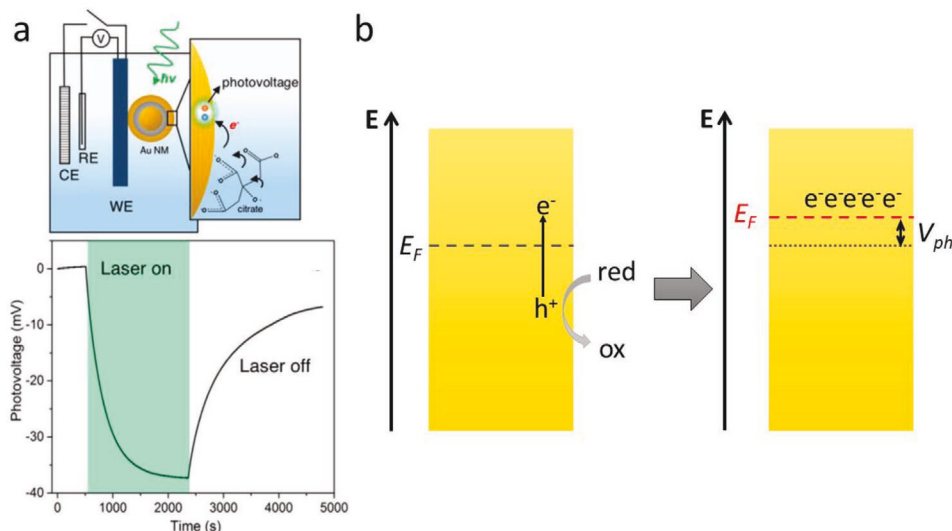
3.1.1. Metal Electrodes

OCP study on plasmonic metal electrodes was firstly reported by Brus group for revealing the mechanism of plasmon-induced growth of Ag nanoprisms.[29] Hot-hole-driven citrate oxidation induced electron accumulation on surfaces and led to a cathodic OCP shift on Ag NP electrodes.[29] It should be noticed that within the resolution of electrochemical response ($\approx$ms – s),[16] hot electrons should relax to the Fermi level before they are detected. Thus, V_{ph} is not an indicator of instant energy levels of hot electrons. Indeed, in this case, hot holes are scavenged, and electrons are accumulated on metal surfaces and raise the Fermi level of the electrode. Hence, V_{ph} reveals the steady-state energy of the thermalized electrons that are accumulated on the electrode. This understanding is further supported by a recent OCP study of citrate oxidation on a Au NP electrode (**Figure 7**a).[30] A V_{ph} less than 40 mV (Figure 7a was observed, which was much lower than theoretical energy levels of hot electrons ($\approx$1 eV).[30–31] This phenomenon confirmed that it was the energy levels of thermalized electrons that dominated V_{ph}, rather than instant energy levels of hot electrons (Figure 7b).

In the absence of hole scavengers, SPR excitation of a bare Au NP electrode only exhibited a low V_{ph} of less than 10 mV.[4a] Recently, it was discovered that surface modification of a Au electrode with a surfactant, poly(vinylpyrrolidone) (PVP) greatly enhanced its V_{ph} (**Figure 8**a).[4a] PVP stabilized hot electrons at Au/PVP interfaces, which left hot holes on Au surfaces. Those holes were compensated by negatively charged ions in the electrolyte (Figure 8b left). This compensation moved Fermi level towards the cathodic direction, causing the enhanced V_{ph} (Figure 8b right). Hence, in the absence of hole scavengers, plasmon-generated V_{ph} on metal NP electrodes reveals the extent of electron-hole separation on metal surfaces.[2d]

3.1.2. Metal/Semiconductor Electrodes

The physical meaning of V_{ph} on metal/semiconductor electrodes is determined by the doping type of semiconductors. Herein, we firstly briefly introduce the classical understanding of photo-induced OCP shift on semiconductor electrodes. When semiconductors come into contact with electrolytes, band bending is formed beneath surfaces as the Fermi level of electrodes equilibrates with redox pairs in electrolytes.[32] For example, for an n-type semiconductor contacted with the electrolyte consisting of OH^-/O_2 as the redox pair, an upward band bending is formed after reaching equilibrium (**Figure 9**a).[33] Upon photo-excitation, the upward band bending sweeps photo-generated holes to surfaces, and those surface-accumulated holes are compensated by negatively charged species in the electrolyte.[34] This compensation diminishes the extent of band bending and increases Fermi level, causing OCP to
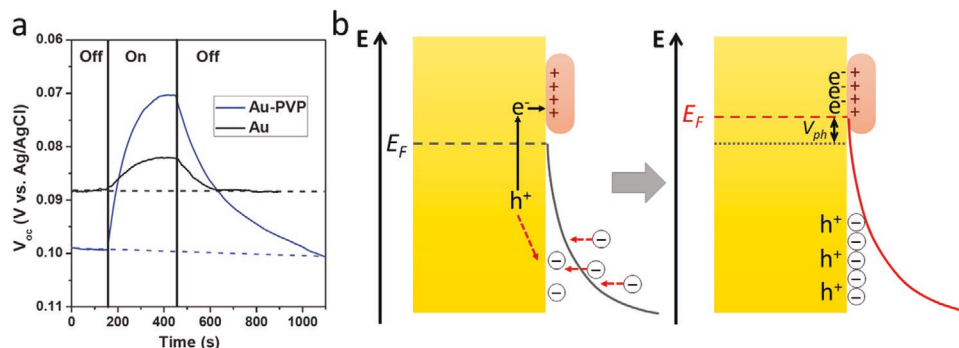
Figure 7. OCP study on metal electrodes in the presence of hole scavengers. a) Top figure: scheme of a PEC cell consisted of a Au NP electrode, in which hot-hole-induced oxidation of citrate resulted in V_{ph}. Bottom figure: V_{ph} versus time of the Au NP electrode before, during, and after 550 nm laser irradiation. b) The schematic of V_{ph} generation on metal electrodes in the presence of hole scavengers. When hot holes are scavenged, hot electrons are accumulated on metal surfaces and raise Fermi level, which is dictated by V_{ph}. (a) Reproduced with permission.[30] Copyright 2017, American Chemical Society.

move towards cathodic direction.[34–35] V_{ph} (i.e., the OCP shift) is dictated by the split of Fermi level into quasi-Fermi levels of electrons (E_{Fn}) and holes (E_{Fp}), where E_{Fp} equilibrates with OH^-/O_2 in the electrolyte (Figure 9b).[33,35] The above description is based on ideal conditions. Experimentally observed V_{ph} is usually smaller due to the presence of surface defects.[33a] For example, the partial Fermi-level pinning effect causes potential loss (η_H) within the Helmholtz layer, which lowers V_{ph} (Figure 9c).[33a] For p-type semiconductors, band bending is downward, which results in electron accumulation on surfaces and charge compensation by positive species from electrolytes. Therefore, OCP moves towards anodic direction under irradiation.[34,36]

Under SPR excitation, cathodic OCP shift occurs on metal/n-type semiconductor electrodes (e.g., Au/TiO₂)[5a] and anodic OCP shift occurs on metal/p-type semiconductor electrodes (e.g., Au/GaN).[23a] The analogous OCP behavior

between semiconductor and metal/semiconductor electrodes indicates that those two types of photoelectrodes share the same working principle in the scope of OCP measurements. That is, surface hole accumulation dominates OCP shift on metal/n-type semiconductor electrodes, while surface electron accumulation dominates that on metal/p-type semiconductor electrodes.

Based on these working principles, we analyze OCP results obtained from widely explored Au/TiO₂ electrodes in detail. Upon SPR excitation, cathodic OCP shift was observed on Au/TiO₂ electrodes, which resulted in a V_{ph} of ≈0.2 V (**Figure 10**a).[5a] The cathodic OCP shift should be attributed to the accumulation of surface-trapped holes, considering that TiO₂ is an n-type semiconductor. Noting that only TiO₂ was in direct contact with the conductive substrate (FTO, Figure 10b for commonly used Au/TiO₂ electrodes).[5a,b] Plasmon-generated hot holes should transfer from Au to

Figure 8. OCP study on metal electrodes in the absence of hole scavengers. a) Influence of PVP on V_{ph} of a Au NP electrode. b) The schematic of V_{ph} generation on metal electrodes in the presence of surfactant (the orange part with capsule shape) that stabilizes hot electrons. Counter ions migrate from electrolytes to the surface of catalyst to compensate hot holes and move up Fermi level. (a) Reproduced with permission.[4a] Copyright 2016, Springer Nature.

ADVANCED
SCIENCE NEWS
www.advancedsciencenews.com

ADVANCED
MATERIALS
www.advmat.de
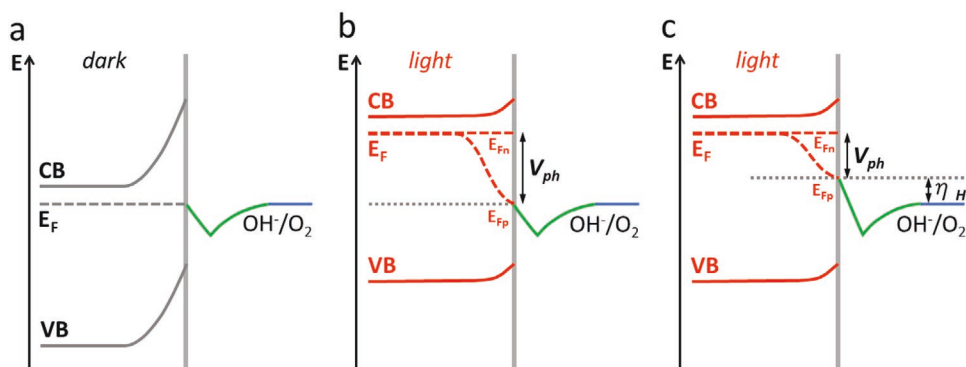
Figure 9. V_{ph} generation on n-type semiconductor electrodes a) in the dark and b) under photo-excitation, and c) in the presence of potential loss (η_H) within the Helmholtz layer. V_{ph} is dictated by the split of Fermi level into semi-Fermi levels of electrons (E_{Fn}) and holes (E_{Fp}), where E_{Fp} equilibrates with redox in electrolytes. Adapted with permission.[33a] Copyright 2015, American Chemical Society.

TiO_2 to be detected (Figure 10b, which implied the presence of surface-trapped holes on TiO_2. Those TiO_2-trapped holes were then compensated by negatively charged species from the electrolyte, which led to the cathodic OCP shift (Figure 10a). A closer observation of the energy diagram at interfaces showed that V_{ph} derived from the split of the Fermi level on TiO_2 into semi-Fermi levels of electrons (E_{Fn}) and holes (E_{Fp}), where E_{Fp} equilibrates with redox in electrolytes (Figure 10b). The aforementioned "transfer and trapping" process accounted for the slow increase of OCP on Au/TiO_2 electrodes upon SPR excitation (Figure 10a). In contrast, an instant increase of OCP was observed on pure TiO_2 photoanodes upon photo-excitation (Figure 10a).[5a] From this viewpoint, OCP measurement is an ideal tool to study hot-hole transfer and trapping on plasmonic metal/semiconductor photoanodes.[2d,20e]

3.2. Closed-Circuit Measurements

Under closed-circuit conditions, only one type of hot carrier (either electron or hole) remains on working electrodes. For photoanodes, hot electrons are swept away from working electrodes and hot holes are left for driving oxidation reactions. Meanwhile, hot holes are removed from photocathodes and hot electrons remain on working electrodes. Such a charge separation prolongs lifetimes of hot carriers and allows for the separated exploration of hole-transfer and electron-transfer dynamics. In this section, three widely used closed-circuit PEC measurements, namely LSV, EIS, and IPCE are discussed for plasmonic photocatalysis.

3.2.1. Linear Sweep Voltammetry

Voltammetry measures currents as a function of applied potentials. PEC research focuses mostly on half-reactions, either on photoanodes or on photocathodes, and the targeting reactions are usually non-reversible (e.g., water reduction and water oxidation). Therefore, LSV (the potential between a working electrode and a reference electrode is swept linearly) is more commonly used than cyclic voltammetry (CV).[3b,5b,10b,c,f,20a] An LSV curve provides two important parameters, i.e., onset
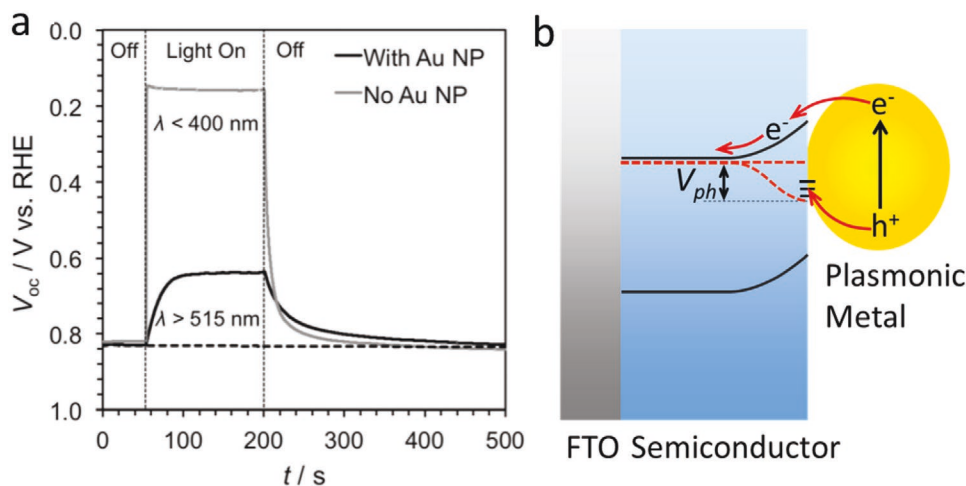
Figure 10. OCP study on metal/semiconductor photoanodes. a) OCP measurements on TiO_2-only (gray) and Au/TiO_2 (black) photoanodes upon exposure to UV or visible-light excitation, respectively. b) The schematic of V_{ph} generation on a metal/semiconductor photoanode. (a) Reproduced with permission.[5a] Copyright 2014, Wiley-VCH.

**ADVANCED
SCIENCE NEWS**

www.advancedsciencenews.com

**ADVANCED
MATERIALS**

www.advmat.de
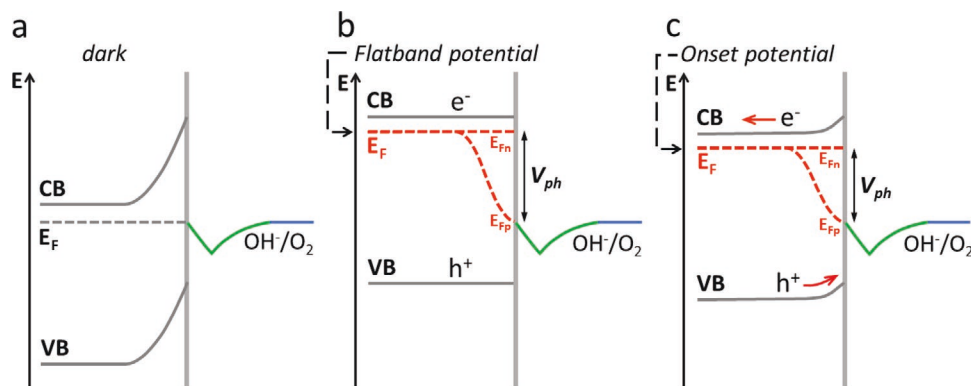
Figure 11. The schematic of onset potential on an n-type semiconductor electrode. Energy diagrams showing a) in the dark and at b) flatband potential and c) onset potential.

potential and photocurrent. Onset potential reflects the interfacial charge-transfer dynamics,[37] while photocurrent is usually taken as an indicator of photoactivities.

Onset potential is determined by flatband potential, overpotential, and V_{ph}.[33] For instance, for an LSV measurement on *n*-type semiconductor photoanodes, the photo-induced electron-hole separation generates V_{ph} that cathodically moves the onset potential from the dark potential (**Figure 11**a) to a value near the flatband potential (Figure 11b). If a bias more anodic than the flatband potential is applied on the photoanode (Figure 11b), an upward band bending forms and drives photogenerated holes to the electrode/electrolyte interfaces (Figure 11c).[37a] An anodic photocurrent appears when the applied bias is further increased.

Onset potential can be used to identify photo-active materials on multiple-component electrodes, as different materials would have distinct flatband potentials and overpotentials under a certain reaction condition. For PEC water oxidation, TiO_2 photoanodes exhibited onset potentials in the range of -0.8 to -0.7 $V_{Ag/AgCl}$ (i.e., $0.2 - 0.3$ V_{RHE}) (**Figure 12**a),[38] while Au electrodes showed more anodic onset potentials around $1.5 - 1.9$ V_{RHE} (Figure 12b).[2d,22c,39] Notably, on Au/TiO_2 photoanodes, when only SPR of Au was excited, onset potentials appeared to be around $0.4 - 0.5$ V_{RHE} (Figure 12b).[2d,5b]

This value was closer to that of TiO_2, strongly suggesting that active sites for hot-hole-induced water oxidation on Au/TiO_2 were related to TiO_2 surfaces.[2d] This result was consistent with our analysis on V_{ph} of Au/TiO_2 electrodes as shown in Section 3.1.

The energy distribution of hot carriers can be estimated from onset potential. In the study of electro-polymerization of aniline on Au NPs photocatalyst (**Figure 13**a), plasmon-generated hot holes were found to reduce onset potentials of aniline polymerization (Figure 13b), and the effective energy of hot holes was estimated from onset potentials under various wavelength (Figure 13c).[40] Photoexcitation at the wavelength of SPR peak region was found to produce the largest decrease in onset potentials, which indicated that hot holes generated from Landau damping (surface-assisted decay) of SPR possessed the highest effective energy (Figure 13c).[40]

In LSV measurements, when sweeping the potential above the onset potential, photocurrents keep increasing with the potential and reaction rates can also be facilitated by the applied potential. On metal NP electrodes, the Fermi level is precisely controlled by the applied potential and thus energy levels of plasmon-excited carriers can be estimated. On the other hand, on metal/semiconductor heterostructure electrodes, the Fermi level of semiconductor is precisely controlled by the applied
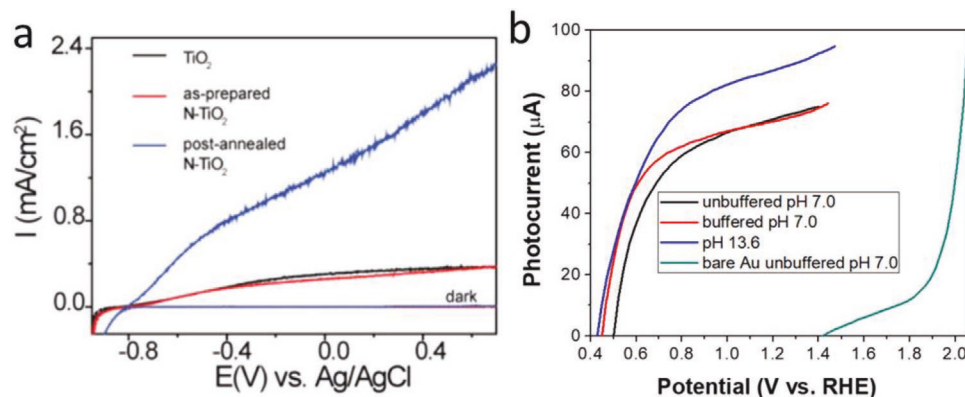
Figure 12. Examples of onset potentials on TiO_2 and Au/TiO_2 photoanodes. a) LSV of TiO_2 photoanodes under 100 mW/cm² Xenon lamp in 1.0 M NaOH aqueous electrolyte. b) LSV of Au/TiO_2 electrodes under visible-light illumination. (a) Reproduced with permission.[38b] Copyright 2015, American Chemical Society. (b) Reproduced with permission.[2d] Copyright 2020, Royal Society of Chemistry.
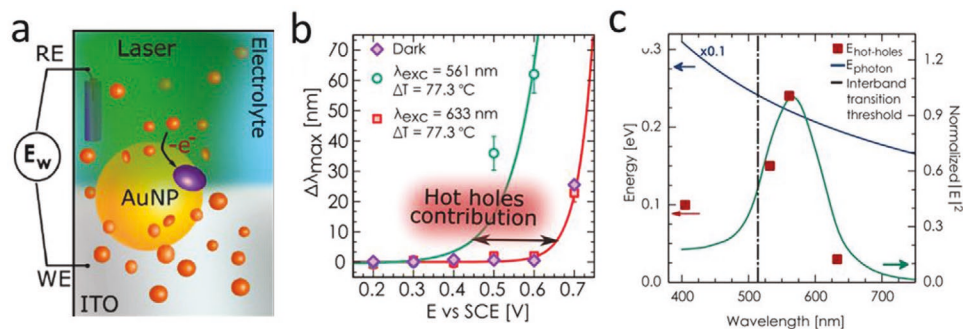
Figure 13. Estimation of energy contribution of hot holes from onset potentials. a) Scheme of electro-polymerization of aniline on Au NPs photocatalyst. b) Red shifts of maximum scattering wavelength ($\Delta\lambda_{max}$) caused by electro-polymerization of aniline as a function of applied potentials (E). Polymerization was monitored optically through $\Delta\lambda_{max}$ in the scattering spectra of AuNPs. c) Energy contribution of hot holes as a function of the incident wavelength, which was estimated from the reduction of onset potential. Reproduced with permission.[40] Copyright 2019, American Chemical Society.

potential and it can be speculated that the Fermi level of metal would follow the trend of that of semiconductor. But it remains unknow whether Fermi levels of metal and semiconductor would synchronize tunes during LSV. To solve this problem, the dual-working electrode technique[41] should be developed for plasmonic metal/semiconductor heterostructures, with which the potentials of both metal and semiconductor can be simultaneously controlled/measured.

In a recent study, the energy distributions of plasmonic holes on Au/TiO$_2$ electrodes (**Figure 14**a) were determined by measuring anodic photocurrents produced in the presence of a series of probe reactants with different redox potentials (Figure 14b).[42] Instead of directly measuring photocurrent on Au/TiO$_2$ electrodes, the current from the oxidation of reactants on a Pt counter microelectrode closely placed to Au/TiO$_2$ electrodes was measured, which indirectly reflected consumption rates of reactants on Au/TiO$_2$ electrodes and the external quantum efficiency (EQE) of hot holes at different energy levels. Energy distributions of hot holes excited under a certain wavelength were further extracted by fitting EQE of hot holes with the Fermi–Dirac function (Figure 14c).[42]

Following LSV measurements, chronoamperometry is usually used to explore detailed photocurrent evolution by holding applied bias at a constant value. Recently, plasmon-increased temperature (i.e., photothermal effect) and the generation of energetic charge carriers (i.e., photoelectronic effect) were disentangled via chronoamperometry and temperature-control

measurements.[25c,43] Photoexcitation of a Au nanoelectrode generated a rapid response current (RRC) and a slow response current (SRC), which were attributed to the photoelectronic effect and photothermal effect, respectively.[43] **Figure 15**a illustrated the PEC process induced by chopped light. Plasmon-generated energetic charge carriers decay in the timescales of ≈ps, which should be reflected immediately via the photocurrent response in the timescales of ≈ms. Contrarily, a significantly longer time (≈s) is necessary to achieve thermal diffusion equilibrium for photothermal effect. Thus, PEC measurement with the time resolution of ≈ms would be able to disentangle those two effects (Figure 15b). Recently, a similar slow photocurrent response was observed on a nanostructured Ag photocathode, which was applied to disentangle hot-carrier effect from photothermal effect.[25c]

3.2.2. Electrochemical Impedance Spectroscopy

EIS is an extensively developed tool for mechanistic research of charge transfer on electrodes.[19e,f] It is a frequency-modulated technique, in which impedance, $Z(\omega)$, of photoelectrode is measured as a function of angular frequency (ω) of perturbations around an applied potential.[44] EIS result is commonly displayed as a Nyquist plot with imaginary impedance ($Z''(\omega)$) as the y-axis and real impedance ($Z'(\omega)$) as the x-axis (**Figure 16**a). In domains with different frequencies, kinetics of
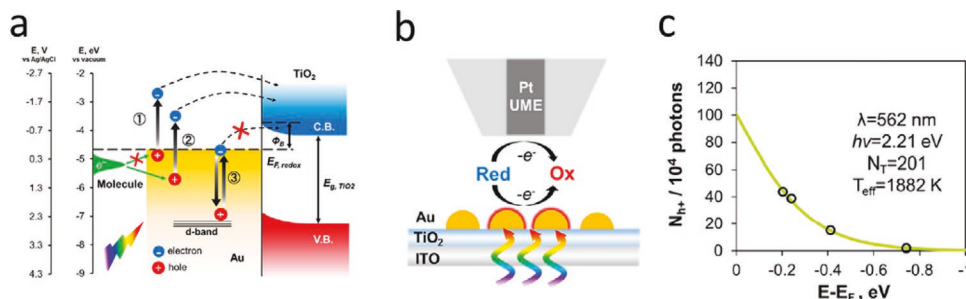
Figure 14. Energy distributions of plasmonic holes. a) The Schematic depicting hot-carrier generation and transfer mechanisms. b) Scanning electrochemical microscopy (SECM) measurement that reflected consumption rates of reactants on Au NP electrodes. c) Populations of hot holes obtained from probe dependent experiments (black symbols) fit to Fermi–Dirac distribution function with excitation wavelengths of 562 ± 20 nm. Reproduced with permission.[42] Copyright 2019, American Chemical Society.

**ADVANCED
SCIENCE NEWS**

www.advancedsciencenews.com

**ADVANCED
MATERIALS**

www.advmat.de
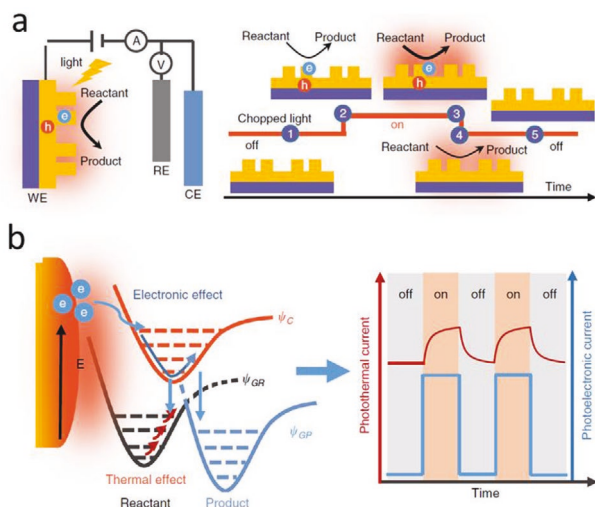
Figure 15. Photocurrent evolution on a Au nanoelectrode array. a) Schematic of PEC characterization under chopped light. b) Schematic of the mechanism for disentangling the photoelectronic effect and photothermal effect of SPR on a Au electrode and the resulted photocurrent evolution. Reproduced with permission.[43] Copyright 2019, Springer Nature.

various charge-transfer steps with the corresponding timescales can be revealed. For example, on semiconductor photoanodes, data obtained in the high-frequency domain is related to surface hole-trapping process, while the low-frequency domain reveals dynamics of interfacial hole transfer involved in surface chemical reactions (Figure 16a).[18a,19b] Based on this property, EIS is used for studying surface states (surface active sites for chemical reactions) on semiconductor photoanodes.[19a,b] A representative electric model (inset in Figure 16a has been developed to extract electrochemical parameters (capacitance and resistance) from EIS results for revealing hole-transfer and hole-trapping dynamics at surface states.[19a,b] A peak in capacitances appeared when the potential used in EIS measurements

was close to the onset potential of photocurrent, representing charging and discharging of surface states.[19a,b] This electrochemical characteristic indicated that interfacial charge transfer took place via surface states.[18a,19a,b] This methodology is promising for detecting hot holes trapped by surface states of semiconductors on plasmonic metal/semiconductor photoanodes. This method was recently applied in the study of PEC water oxidation on Au/TiO$_2$ photoanodes (Figure 16b).[2d] In this work, by combining LSV, OCP measurements and EIS analysis, the photo-generated holes on Au were demonstrated to transfer to and be trapped on TiO$_2$. From the time constant values of EIS results, the TiO$_2$-trapped holes exhibited a long lifetime that was able to drive the sluggish water oxidation.[2d]

3.2.3. Incident Photon-to-Electron Conversion Efficiency

IPCE displays activities of photoelectrodes at given wavelengths. For photoelectrodes containing semiconductors, due to the significant capacitive charging current during voltammetry, photocurrent measured in LSV cannot accurately represent activities. Therefore, a common way to perform IPCE study is to use the steady-state photocurrent at a certain constant potential as an indicator of the accurate reaction activity.[10b,c,13c] IPCE measurements can also utilize diverse indexes such as reaction activities, e.g., V_{ph}.[30] In plasmonic photocatalysis, numerous works reported that IPCE results reproduced corresponding SPR spectra, which were used to support plasmon-driven reaction mechanisms.[5b,10b,c,f,13b,c,20b,23b,45]
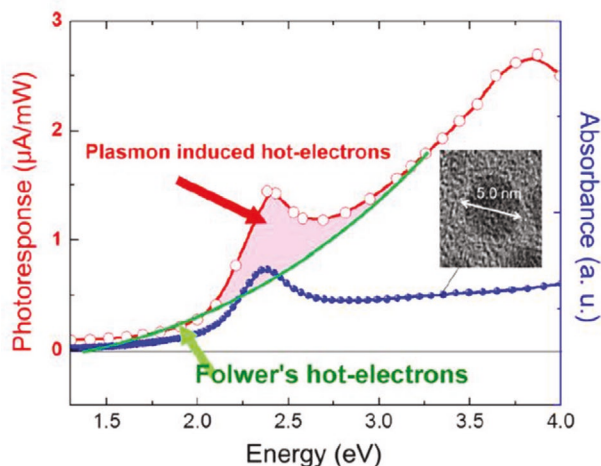
On metal/semiconductor photoanodes, IPCE results were proposed to follow Fowler theory adapted by SPR spectra[13b,20b]

$$IPCE \approx C_F \frac{(h\nu - q\phi_B)^2}{h\nu} S(\nu) \tag{1}$$

where C_F is the Fowler emission coefficient, $h\nu$ is the energy of excitation light, $q\phi_B$ is the Schottky barrier height, and $S(\nu)$ is the SPR absorption spectrum.
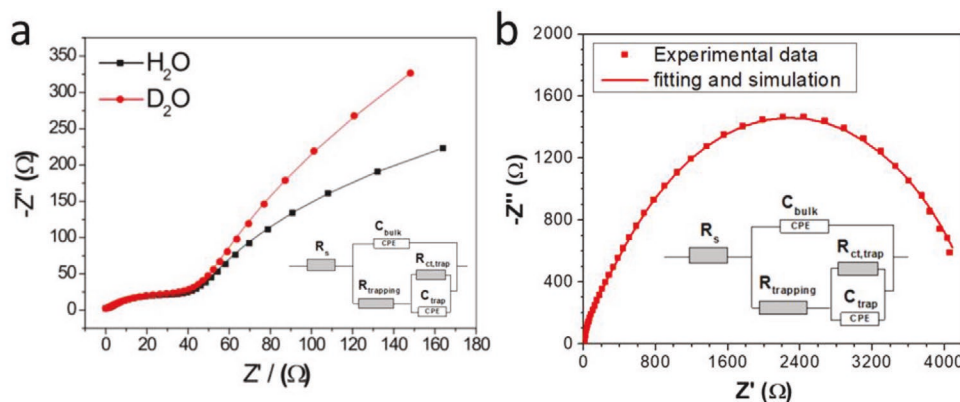
Figure 16. Examples of EIS study on semiconductor and metal/semiconductor photoanodes. a) Nyquist plots for EIS conducted in H$_2$O and D$_2$O on a hematite photoanode at 1.23 V$_{RHE}$ in an unbuffered electrolyte at pH/pD 10.0. Nyquist plots exhibit two semicircles. The high-frequency semicircle represented hole trapping by surface states, while the low-frequency semicircle illustrated interfacial holes transfer. (insert) Model circuit for EIS fitting. In this model, $R_{trapping}$ represented resistance of surface hole-trapping process, C_{trap} represented amount of charges accumulated at surface states, and $R_{ct,trap}$ represented resistance of interfacial charge transfer. b) A representative Nyquist plot obtained from the EIS measurement of a Au/TiO$_2$ electrode. (a) Reproduced with permission.[18a] Copyright 2016, American Chemical Society. Reproduced with permission.[2d] Copyright 2020, Royal Society of Chemistry.

Figure 17. IPCE on a metal/semiconductor photoanode. The absorption spectrum of a Au/ZnO photoanode (blue) and plots of photocurrent versus irradiation energy (red). Reproduced with permission.[20b] Copyright 2012, American Chemical Society.

This theory indicates that photocurrent in an IPCE measurement is proportional to the number of energetic hot electrons that transfer across the Schottky barrier. **Figure 17** displays a typical IPCE result of PEC water oxidation on a Au/ZnO photoanode and the photo-response well reproduced the absorbance of catalysts.[20b] Apart from the IPCE peak derived from "Plasmon-induced hot-electrons," a "baseline" that continuously increased with irradiation energy (Figure 17) was also observed. It is noteworthy that on plasmonic Au NPs, an increasing portion of interband transition occurred at a shorter wavelength, which generated more energetic holes and less energetic electrons. In addition, as mentioned in Section 2.1 hot-hole transfer should be RDS for PEC water oxidation on photoanodes. Therefore, "hotter holes" generated by interband transition at a shorter wavelength were more efficient in driving water oxidation, which caused a larger number of electrons to be transferred to semiconductor, leading to increasing photocurrent in IPCE. Hence, efficiencies of surface hole-driven reactions dominated IPCE results on plasmonic photoanodes.

The hole-driven mechanism was clearly confirmed by a recent IPCE study of citrate oxidation on a Au NP photoanode.[30] A weak correspondence between the photo-oxidation activity of citrate and extinction spectrum of a Au NP electrode was reported (**Figure 18**a). To account for this IPCE trend, researchers developed a model by simultaneously considering the spatial and energetic overlap among photon absorption of Au NPs, hot-carrier energy distribution, and the HOMO level of citrate (Figure 18b).[30] Hot holes generated via interband excitation and warm holes generated via intraband excitation were considered to contribute to the high and low V_{ph} observed at short and long wavelength regions, respectively (Figure 18b).[30] In addition to this general trend, throughout the whole spectrum, IPCE peaks matching with SPR peaks remained, which were derived from the substantial amount of hot holes generated within the SPR peak range.

On photocathodes where hot-electron transfer dominated RDS rather than hot-hole transfer, interband transition at short wavelength did not result in higher photocurrent, owing to "cold" electrons generated in this region. On the contrary, in wavelength region near SPR peaks, intraband transition from SPR decay generated hot electrons that were energetically sufficient for driving target reactions, which caused the IPCE shape to reproduce SPR extinction spectrum (**Figure 19**).[23b]

In summary, IPCE shows the number of hot carriers with sufficient energy to drive targeting reactions. For photoanodes, hot holes dominate IPCE results, while for photocathodes, hot electrons dominate. Combined with absorption spectra, IPCE measurement can be used to investigate energetics of hot carriers.

3.3. Spectroelectrochemistry

SEC studies have only emerged in plasmonic photochemistry in recent years.[46] Through this technique, optical spectroscopies are integrated with PEC cells, and captured spectra are used as additional indicators to normal electrochemical ones to monitor chemical processes. **Figure 20** shows a typical set-up of an SEC system.[46a] Main components of a SEC cell are
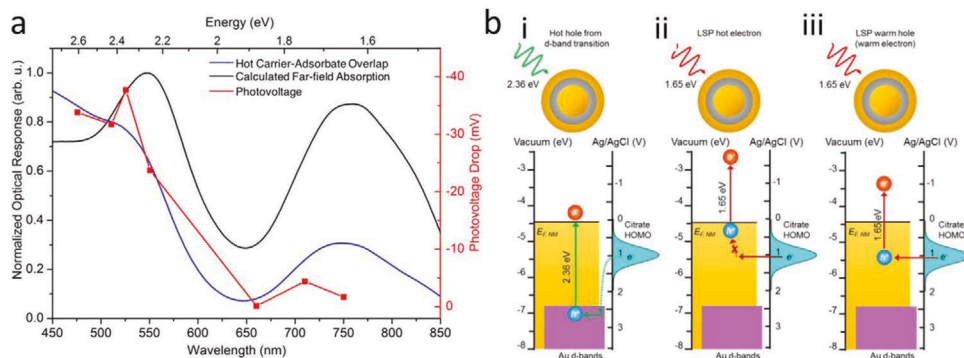
Figure 18. IPCE results on a Au NP photoanode. a) Measured V_{ph} from a Au NP electrode (red squares), which was plotted as a function of excitation wavelength. Calculated far-field absorption of Au ensemble was shown in black and calculated hot carrier–adsorbate overlap was shown in blue. b) Schemes depicting hot-hole-driven citrate oxidation. i) A 2.36 eV excitation resulted in the generation of a hot hole within Au d band, which exergonically obtained electrons from HOMO of citrate. ii) A 1.65 eV excitation resulted in the formation of a hot electron but left a cold hole near the Fermi level misaligned with the HOMO level. iii) A warmer hole generated under a 1.65 eV excitation, which overlapped with the HOMO level of citrate that facilitated hole transfer. Reproduced with permission.[30] Copyright 2017, American Chemical Society.

ADVANCED
SCIENCE NEWS
www.advancedsciencenews.com

ADVANCED
MATERIALS
www.advmat.de
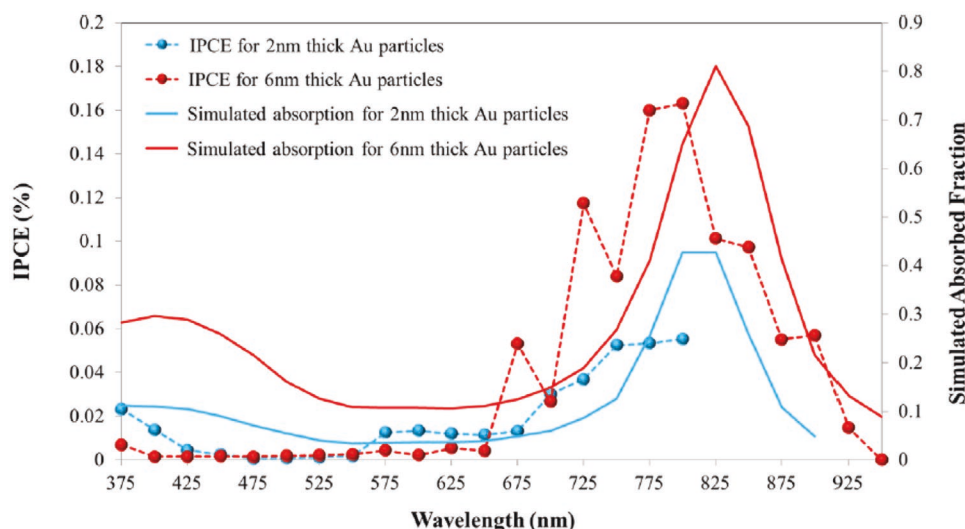
Figure 19. An IPCE study on a metal/semiconductor photocathode. Comparison between measured IPCE (left axis) and simulated absorption spectra (right axis) for 2 nm (blue) and 6 nm (red) thick Au NP electrodes. Reproduced with permission.[23b] Copyright 2015, American Chemical Society.

a chip-form plasmonic PEC cell and an aligned optical detector (objective). The objective collects optical spectra of plasmonic NPs on a working electrode during electrochemical experiments. Scattering, absorption, or extinction (absorption + scattering) spectra can be collected. Variations in spectral characteristics, including peak position, intensity, and full-width at half maximum (FWHM), are used to reveal relevant electrochemical processes.

Optical properties of plasmonic metal NPs change with dielectric constant of surrounding materials, which can be monitored with SEC measurements.[46a,47] In a simplified model containing metal spheres, the extinction spectrum is depicted as[3c]

$$E(\lambda) = \frac{24\pi^2 N a^3 \varepsilon_{out}^{3/2}}{\lambda \ln(10)} \left[\frac{\varepsilon_i(\lambda)}{\left(\varepsilon_r(\lambda) + 2\varepsilon_{out}\right)^2 + \varepsilon_i^2(\lambda)} \right] \quad (2)$$

Here, a represents the radius of a metal sphere, N is the number of conducting electrons, and ε_{out} is the dielectric constant of surrounding environment. In the square bracket,
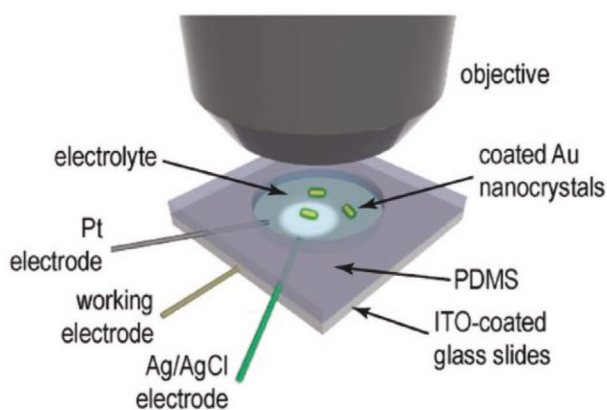
**Figure 20.** Set-up of a typical SEC cell. Reproduced with permission.[46a] Copyright 2016, Wiley-VCH.

ε_i and ε_r are imaginary and real parts of metal dielectric function, respectively. It can be read from the equation that for metal nanospheres, an extinction peak appears when ε_r is close to $-2\varepsilon_{out}$ (i.e., $\varepsilon_r(\lambda) + 2\varepsilon_{out} \approx 0$). When physical or chemical properties of surrounding material (i.e., ε_{out}) vary, the wavelength that fulfills $\varepsilon_i(\lambda) \approx -2\varepsilon_{out}$ varies accordingly, which is reflected as a shift in the extinction peak. Such a peak shift ($\Delta\lambda_{max}$) can be quantitatively described by the following[3c]

$$\Delta\lambda_{max} = m\Delta n \left[1 - \exp(-2d / l_d) \right] \quad (3)$$

Here, m represents the bulk refractive index of metal NPs, Δn is the change of refractive index of surrounding materials ($n = \varepsilon^{1/2}$), d is the effective thickness of surrounding materials, and l_d is the electric field decay length.

In electrochemical studies, surface chemical reactions driven by applied bias would alter chemical environment of electrode surfaces. When an electrode is composed of plasmonic metal NPs, SEC measurements can serve as a useful tool to track those surface reactions by monitoring SPR peak shift with respect to applied bias. For example, on Au nanorods coated with polyaniline, a ≈100 nm red shift was observed when polyaniline transformed to reduced form under negative applied potentials. This shift was attributed to the increasing real part of refractive index of polyaniline in the reduced form (**Figure 21**a).[46a] Spectral changes of this nature can also be applied for mechanistic investigations. A red shift in extinction peaks of Au nanorods occurred under light irradiation and positive bias as a result of altered refractive index of oxidized surface.[46d] Through monitoring the change of extinction peak shift along with irradiation wavelengths and pHs of solutions, it was concluded that the oxidation of Au was caused by surface hot-hole accumulation and the resulted lowered Fermi level of Au NPs.[46d]

Recent SEC studies uncovered other surface events (e.g., interparticle interactions) that would alter optical properties of plasmonic metal NPs.[46b,c] For example, optical coupling between Au NPs and a Au thin film generated charge-transfer plasmon
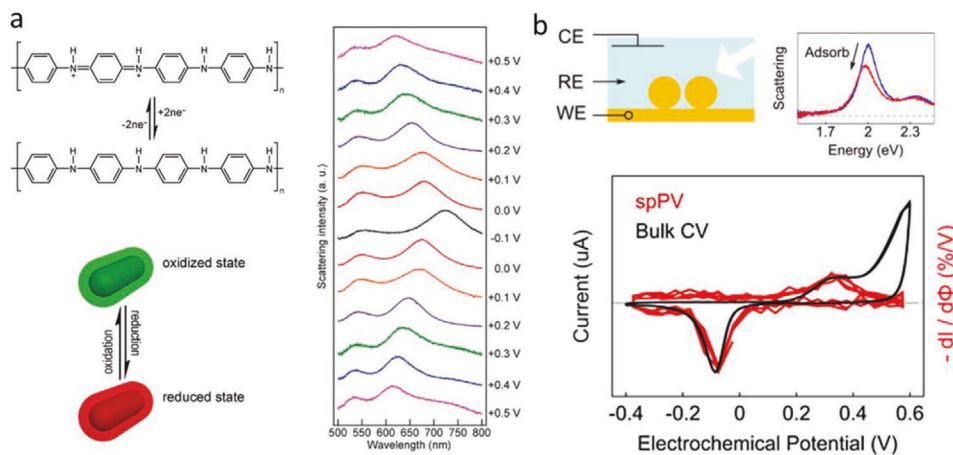
Figure 21. Examples of SEC studies. a) SPR peak shift of polyaniline-coated Au nanorods when polyaniline transformed from oxidized to reduced form when the applied potential was changed from positive to negative. b) Detection of sulfate anion adsorption on Au NPs/Au thin film. The scattering peak intensity from CT mode decreased as a result of sulfate anion adsorption (top right figure). Adsorption/desorption of anions on the Au thin film was detected by monitoring either current (normal CV, black curve in the bottom figure) or scattering peak intensity of CT mode (SEC, red curve) at different applied potentials. SEC eliminated the impact from H_2 evolution that had a peak overlapping with the desorption peak of anions in normal CV measurements (black curve). (a) Reproduced with permission.[46a] Copyright 2016, Wiley-VCH. (b) Reproduced with permission.[46b] Copyright 2016, American Chemical Society.

modes (CT modes) that were sensitive to the physical property of Au NPs and films.[46b] This allowed the detection of potential-controlled anion adsorption and desorption on a Au NP/Au thin film system by monitoring spectral change of CT modes.[46b] Adsorption of anions decreased the conductivity of Au thin film, which weakened the coupling between Au NPs and the Au thin film and caused a decrease of scattering peak intensity from CT modes (Figure 21b).[46b] Such adsorption/desorption processes cannot be clearly identified by normal electrochemical measurements (e.g., CV), as its signal would be mixed with that from deprotonation and H_2 evolution reaction (Figure 21b).

Optical properties of plasmonic metal NPs also depend on their own electron density, according to[48]

$$\omega_p^2 = \sqrt{\frac{Ne^2}{m_e \varepsilon_0}} \tag{4}$$

Here, ω_p is the inherent plasmon frequency of a metal in vacuum, N represents the electron density of metal NPs, ε_0 is the permittivity of free space, and e and m_e are the charge and mass of an electron, respectively.

Both red shift and broadening of absorption peaks of Au NP electrodes were observed after charging them with positive bias (reducing electron density N).[46e] It is anticipated that integrating the electron-density-dependent optical property with photochemical reactions would provide additional opportunities to disclose their mechanistic information. However, the inherent high electron density within metal NPs limits their sensitivity in detecting chemical reactions that involve carrier transfer between reactants and metal NPs, as the number of transferred carriers is negligible compared to the number of electrons in metal NPs. In contrast, novel plasmonic materials based on doped semiconductors show higher potential in this aspect. Doped semiconductors gain their plasmonic effect from free majority charge carriers (either electrons or holes), whose population is lower than that of free electrons in metal NPs by orders of magnitude.[49] This property

renders semiconductor NPs more sensitive towards electrochemical charging, which is beneficial for detecting chemical reactions. For example, the oxidation of methyl viologen (MV) on $Cu_{2-x}S$ nanocrystals was monitored with high sensitivity by measuring SPR absorption of $Cu_{2-x}S$.[50] The SPR absorption disappeared when $Cu_{2-x}S$ accepted electrons from MV and recovered when $Cu_{2-x}S$ donated extra electrons to oxygen. Such a reversible switch-on and switch-off of SPR property provides a promising platform to monitor chemical reactions.

The sensitivity of doped semiconductor NPs for SEC measurements is closely related to sizes of NPs.[51] For instance, a recent study reported that for Sn-doped In_2O_3 ($Sn:In_2O_3$) NPs, the sensitivity of SPR modulation by electrochemical charging decreased when sizes or doping levels of NPs became larger (**Figure 22**).[51] In other words, a more significant SPR peak shift and intensity enhancement were observed on smaller and lower-doped $Sn:In_2O_3$ NPs. This was attributed to the formation of a larger depletion region near surfaces for these NPs. The depletion region formed on NP surfaces as a result of the inherently low free-charge carrier density in semiconductors and Fermi level pinning caused by surface defects. The depletion region had an even lower charge carrier density compared with the bulk region, which enabled it to give a more sensitive response to the change in local free charge carrier density. Therefore, $Sn:In_2O_3$ NPs with larger depletion region exhibited higher sensitivity towards electrochemical charging. It was noticed that while most semiconductor NPs have SPR absorption in mid to far-IR region with relatively broad width, fabrication of larger and highly-doped NPs is commonly required to tune their SPR absorption to near-IR or even visible range with a narrower width. However, the above-mentioned study indicated that these tuning processes may sacrifice spectral sensitivity of semiconductor NPs. Such a sophisticated dependence of sensitivity on physical and chemical properties of NPs is not observed in SEC studies based on plasmonic metal NPs, which calls for special attention in future SEC applications involving doped semiconductor NPs.
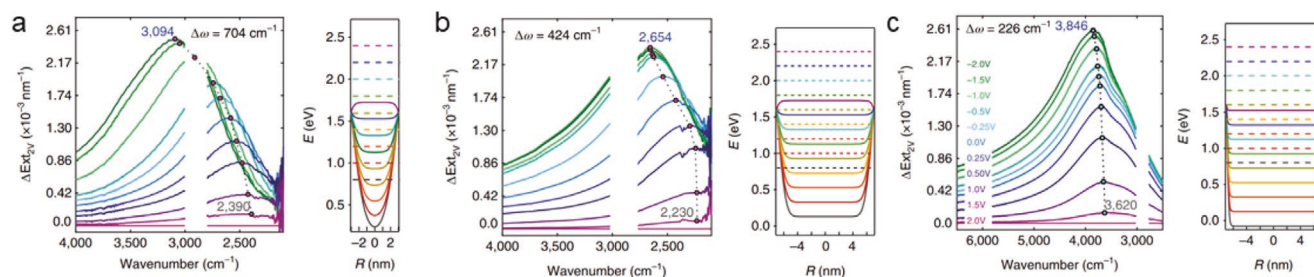
Figure 22. SPR modulation on doped semiconductors. Different sensitivities of SPR modulation by applied bias on a) 1% doped 7.4 nm, b) 10% doped 7.4 nm, and c) 10% doped 11.5 nm Sn:In$_2$O$_3$ NPs. Overall peak shifts decreased from (a–c) because the size and doping level increased. Reproduced with permission.[51] Copyright 2018, Springer Nature.

4. Conclusion

In this review, distinct mechanisms of hot-electron transfer and hot-hole transfer are verified for plasmonic photoelectrochemistry. We provide a comprehensive discussion on both hot-electron and hot-hole transfers to accurately interpret plasmonic photoelectrochemistry. Discussions are mainly focused on PEC measurements on photoanodes. Under open-circuit conditions, both hot-hole and hot-electron transfers contribute to the V_{ph} generation on plasmonic electrodes. Under closed-circuit conditions, as electron transfer is controlled by the potentiostat, hole transfer and accumulation on electrode surfaces dominate the reaction rates and mechanisms. After verifying distinct roles of hot holes and hot electrons, physical locations of active sites and energetics of hot carriers can be revealed from PEC measurements. It is expected that these clarified working principles would benefit mechanistic research of hot-carrier transfer in plasmonic photocatalysis. Finally, photothermal effect should be carefully considered in plasmon-driven photochemical reactions. To date, only very few studies have explored photothermal effect in plasmonic PEC measurements,[52] which needs to be addressed in future studies.

Conflict of Interest

The authors declare no conflict of interest.

[1] Y. Zhang, S. He, W. Guo, Y. Hu, J. Huang, J. R. Mulcahy, W. D. Wei, *Chem. Rev.* **2018**, *118*, 2927.

[2] a) M. L. Brongersma, N. J. Halas, P. Nordlander, *Nat. Nanotechnol.* **2015**, *10*, 25; b) S. Linic, P. Christopher, D. B. Ingram, *Nat. Mater.* **2011**, *10*, 911; c) P. Christopher, M. Moskovits, *Annu. Rev. Phys. Chem.* **2017**, *68*, 379; d) Y. Zhang, Y. Zhang, W. Guo, A. C. Johnston-Peck, Y. Hu, X. Song, W. D. Wei, *Energy Environ. Sci.* **2020**, *13*, 1501.

[3] a) P. Zhang, T. Wang, J. Gong, *Adv. Mater.* **2015**, *27*, 5328; b) S. C. Warren, E. Thimsen, *Energy Environ. Sci.* **2012**, *5*, 5133; c) K. A. Willets, R. P. Van Duyne, *Annu. Rev. Anal. Chem.* **2007**, *58*, 267; d) P. L. Stiles, J. A. Dieringer, N. C. Shah, R. R. Van Duyne, *Annu. Rev. Anal. Chem.* **2008**, *1*, 601.

[4] a) Y. Zhai, J. S. DuChene, Y.-C. Wang, J. Qiu, A. C. Johnston-Peck, B. You, W. Guo, B. DiCiaccio, K. Qian, E. W. Zhao, F. Ooi, D. Hu, D. Su, E. A. Stach, Z. Zhu, W. D. Wei, *Nat. Mater.* **2016**, *15*, 889; b) J. Polte, R. Erler, A. F. Thünemann, S. Sokolov, T. T. Ahner, K. Rademann, F. Emmerling, R. Kraehnert, *ACS Nano* **2010**, *4*, 1076; c) F. L.e Formal, S. R. Pendlebury, M. Cornuz, S. D. Tilley, M. Grätzel, J. R. Durrant, *J. Am. Chem. Soc.* **2014**, *136*, 2564; d) A. J. Cowan, W. Leng, P. R. F. Barnes, D. R. Klug, J. R. Durrant, *Phys. Chem. Chem. Phys.* **2013**, *15*, 8772; e) S. R. Pendlebury, M. Barroso, A. J. Cowan, K. Sivula, J. Tang, M. Gratzel, D. Klug, J. R. Durrant, *Chem. Commun.* **2011**, *47*, 716; f) A. J. Cowan, J. Tang, W. Leng, J. R. Durrant, D. R. Klug, *J. Phys. Chem. C* **2010**, *114*, 4208; g) J. Tang, J. R. Durrant, D. R. Klug, *J. Am. Chem. Soc.* **2008**, *130*, 13885.

[5] a) J. S. DuChene, B. C. Sweeny, A. C. Johnston-Peck, D. Su, E. A. Stach, W. D. Wei, *Angew. Chem., Int. Ed.* **2014**, *53*, 7887; b) S.-F. Hung, F.-X. Xiao, Y.-Y. Hsu, N.-T. Suen, H.-B. Yang, H. M. Chen, B. Liu, *Adv. Eng. Mater.* **2016**, *6*, 1501339; c) K. Qian, B. C. Sweeny, A. C. Johnston-Peck, W. Niu, J. O. Graham, J. S. DuChene, J. Qiu, Y.-C. Wang, M. H. Engelhard, D. Su, E. A. Stach, W. D. Wei, *J. Am. Chem. Soc.* **2014**, *136*, 9842; d) M. W. Knight, H. Sobhani, P. Nordlander, N. J. Halas, *Science* **2011**, *332*, 702; e) C. Clavero, *Nat. Photonics* **2014**, *8*, 95; f) Y. Tian, T. Tatsuma, *Chem. Commun.* **2004**, 1810; g) S. K. Cushing, N. Wu, *J. Phys. Chem. Lett.* **2016**, *7*, 666.

[6] A. Furube, L. Du, K. Hara, R. Katoh, M. Tachiya, *J. Am. Chem. Soc.* **2007**, *129*, 14852.

[7] S. Wang, Y. Gao, S. Miao, T. Liu, L. Mu, R. Li, F. Fan, C. Li, *J. Am. Chem. Soc.* **2017**, *139*, 11771.

[8] a) G. Liu, C. Zhen, Y. Kang, L. Wang, H.-M. Cheng, *Chem. Soc. Rev.* **2018**, *47*, 6410; b) R. Chen, S. Pang, H. An, J. Zhu, S. Ye, Y. Gao, F. Fan, C. Li, *Nat. Energy* **2018**, *3*, 655.

[9] R. Godin, A. Kafizas, J. R. Durrant, *Curr. Opin. Electrochem.* **2017**, *2*, 136.

[10] a) Y. Tian, T. Tatsuma, *J. Am. Chem. Soc.* **2005**, *127*, 7632; b) Y. Nishijima, K. Ueno, Y. Yokota, K. Murakoshi, H. Misawa, *J. Phys. Chem. Lett.* **2010**, *1*, 2031; c) Y. Nishijima, K. Ueno, Y. Kotake, K. Murakoshi, H. Inoue, H. Misawa, *J. Phys. Chem. Lett.* **2012**, *3*, 1248; d) I. Thomann, B. A. Pinaud, Z. Chen, B. M. Clemens, T. F. Jaramillo, M. L. Brongersma, *Nano Lett.* **2011**, *11*, 3440; e) E. Thimsen, F. L.e Formal, M. Grätzel, S. C. Warren, *Nano Lett.* **2011**, *11*, 35; f) J. Lee, S. Mubeen, X. Ji, G. D. Stucky, M. Moskovits, *Nano Lett.* **2012**, *12*, 5014; g) S. Mubeen, J. Lee, N. Singh, S. Kramer,

G. D. Stucky, M. Moskovits, *Nat. Nanotechnol.* **2013**, *8*, 247; h) E. R. Corson, E. B. Creel, R. Kostecki, B. D. McCloskey, J. J. Urban, *iScience* **2020**, 23, 100911; i) H. Li, S. Wang, F. Hong, Y. Gao, B. Zeng, R. S. Haider, F. Fan, J. Huang, C. Li, *J. Chem. Phys.* **2020**, *152*, 194702.

[11] a) T. Tatsuma, H. Nishi, T. Ishida, *Chem. Sci.* **2017**, *8*, 3325; b) E. Kazuma, T. Tatsuma, *Adv. Mater. Interfaces* **2014**, *1*, 1400066; c) H. Minamimoto, T. Toda, R. Futashima, X. Li, K. Suzuki, S. Yasuda, K. Murakoshi, *J. Phys. Chem. C* **2016**, *120*, 16051.

[12] K. Suzuki, X. Li, Y. Wang, F. Nagasawa, K. Murakoshi, *ACS Energy Lett.* **2020**, *5*, 1252.

[13] a) B. Y. Zheng, H. Zhao, A. Manjavacas, M. McClain, P. Nordlander, N. J. Halas, *Nat. Commun.* **2015**, *6*, 7797; b) M. Valenti, A. Venugopal, D. Tordera, M. P. Jonsson, G. Biskos, A. Schmidt-Ott, W. A. Smith, *ACS Photonics* **2017**, *4*, 1146; c) A. Naldoni, U. Guler, Z. Wang, M. Marelli, F. Malara, X. Meng, L. V. Besteiro, A. O. Govorov, A. V. Kildishev, A. Boltasseva, V. M. Shalaev, *Adv. Opt. Mater.* **2017**, 1601031.

[14] X. Meng, Q. Yu, T. Wang, G. Liu, K. Chang, P. Li, L. Liu, J. Ye, *APL Mater.* **2015**, *3*, 104401.

[15] J. B. Khurgin, *Nat. Nanotechnol.* **2015**, *10*, 2.

[16] F. K. Maina, M. Khalid, A. K. Apawu, T. A. Mathews, *JoVE* **2012**, *59*, e3464.

[17] D. C. Ratchford, A. D. Dunkelberger, I. Vurgaftman, J. C. Owrutsky, P. E. Pehrsson, *Nano Lett.* **2017**, *17*, 6047.

[18] a) Y. Zhang, H. Zhang, H. Ji, W. Ma, C. Chen, J. Zhao, *J. Am. Chem. Soc.* **2016**, *138*, 2705; b) Y. Zhang, H. Zhang, A. Liu, C. Chen, W. Song, J. Zhao, *J. Am. Chem. Soc.* **2018**, *140*, 3264.

[19] a) B. Klahr, S. Gimenez, F. Fabregat-Santiago, J. Bisquert, T. W. Hamann, *Energy Environ. Sci.* **2012**, *5*, 7626; b) B. Klahr, S. Gimenez, F. Fabregat-Santiago, T. Hamann, J. Bisquert, *J. Am. Chem. Soc.* **2012**, *134*, 4294; c) A. J. Bard, A. B. Bocarsly, F. R. F. Fan, E. G. Walton, M. S. Wrighton, *J. Am. Chem. Soc.* **1980**, *102*, 3671; d) B. Klahr, S. Gimenez, F. Fabregat-Santiago, J. Bisquert, T. W. Hamann, *J. Am. Chem. Soc.* **2012**, *134*, 16693; e) L. Bertoluzzi, J. Bisquert, *J. Phys. Chem. Lett.* **2012**, *3*, 2517; f) L. Bertoluzzi, J. Bisquert, *J. Phys. Chem. Lett.* **2017**, *8*, 172.

[20] a) K. Ueno, T. Oshikiri, H. Misawa, *ChemPhysChem* **2016**, *17*, 199; b) H. M. Chen, C. K. Chen, C.-J. Chen, L.-C. Cheng, P. C. Wu, B. H. Cheng, Y. Z. Ho, M. L. Tseng, Y.-Y. Hsu, T.-S. Chan, J.-F. Lee, R.-S. Liu, D. P. Tsai, *ACS Nano* **2012**, *6*, 7362; c) Z. Liu, W. Hou, P. Pavaskar, M. Aykol, S. B. Cronin, *Nano Lett.* **2011**, *11*, 1111; d) P. Peerakiatkhajohn, J.-H. Yun, H. Chen, M. Lyu, T. Butburee, L. Wang, *Adv. Mater.* **2016**, *28*, 6405; e) Y.-C. Pu, G. Wang, K.-D. Chang, Y. Ling, Y.-K. Lin, B. C. Fitzmorris, C.-M. Liu, X. Lu, Y. Tong, J. Z. Zhang, Y.-J. Hsu, Y. Li, *Nano Lett.* **2013**, *13*, 3817; f) J. Li, S. K. Cushing, P. Zheng, F. Meng, D. Chu, N. Wu, *Nat. Commun.* **2013**, *4*, 2651; g) M. Zhu, X. Cai, M. Fujitsuka, J. Zhang, T. Majima, *Angew. Chem., Int. Ed.* **2017**, *56*, 2064; h) T. Oshikiri, K. Ueno, H. Misawa, *Angew. Chem., Int. Ed.* **2014**, *53*, 9802.

[21] a) N. Sivasankar, W. W. Weare, H. Frei, *J. Am. Chem. Soc.* **2011**, *133*, 12976; b) L. Duan, F. Bozoglian, S. Mandal, B. Stewart, T. Privalov, A. Llobet, L. Sun, *Nat. Chem.* **2012**, *4*, 418.

[22] a) C. Wang, X.-G. Nie, Y. Shi, Y. Zhou, J.-J. Xu, X.-H. Xia, H.-Y. Chen, *ACS Nano* **2017**, *11*, 5897; b) H. Yang, Z.-H. Wang, Y.-Y. Zheng, L.-Q. He, C. Zhan, X. Lu, Z.-Q. Tian, P.-P. Fang, Y. Tong, *J. Am. Chem. Soc.* **2016**, *138*, 16204; c) G. Liu, P. Li, G. Zhao, X. Wang, J. Kong, H. Liu, H. Zhang, K. Chang, X. Meng, T. Kako, J. Ye, *J. Am. Chem. Soc.* **2016**, *138*, 9128; d) H. Huang, J. Zou, J.-Y. Ye, Z.-Y. Zhou, Z. Lin, X. Kang, P. K. Jain, S. Chen, *Angew. Chem., Int. Ed.* **2019**, *58*, 8794.

[23] a) J. S. DuChene, G. Tagliabue, A. J. Welch, W.-H. Cheng, H. A. Atwater, *Nano Lett.* **2018**, *18*, 2545; b) H. Robatjazi, S. M. Bahauddin, C. Doiron, I. Thomann, *Nano Lett.* **2015**, *15*, 6155.

[24] a) M. Bernardi, J. Mustafa, J. B. Neaton, S. G. Louie, *Nat. Commun.* **2015**, *6*, 7044; b) R. Sundararaman, P. Narang, A. S. Jermyn, W. A. Goddard Iii, H. A. Atwater, *Nat. Commun.* **2014**, *5*, 5788.

[25] a) Y. Kim, E. B. Creel, E. R. Corson, B. D. McCloskey, J. J. Urban, R. Kostecki, *Adv. Eng. Mater.* **2018**, *8*, 1800363; b) A. J. Wilson, V. Mohan, P. K. Jain, *J. Phys. Chem. C* **2019**, *123*, 29360; c) W. Ou, B. Zhou, J. Shen, T. W. Lo, D. Lei, S. Li, J. Zhong, Y. Y. Li, J. Lu, *Angew. Chem., Int. Ed.* **2020**, *59*, 6790.

[26] X. Cui, C. Tang, Q. Zhang, *Adv. Eng. Mater.* **2018**, *8*, 1800369.

[27] a) J. Yang, Y. Guo, R. Jiang, F. Qin, H. Zhang, W. Lu, J. Wang, J. C. Yu, *J. Am. Chem. Soc.* **2018**, *140*, 8497; b) H. Jia, A. Du, H. Zhang, J. Yang, R. Jiang, J. Wang, C.-y. Zhang, *J. Am. Chem. Soc.* **2019**, *141*, 5083.

[28] C. Hu, X. Chen, J. Jin, Y. Han, S. Chen, H. Ju, J. Cai, Y. Qiu, C. Gao, C. Wang, Z. Qi, R. Long, L. Song, Z. Liu, Y. Xiong, *J. Am. Chem. Soc.* **2019**, *141*, 7807.

[29] a) P. L. Redmond, X. Wu, L. Brus, *J. Phys. Chem. C* **2007**, *111*, 8942; b) P. L. Redmond, L. E. Brus, *J. Phys. Chem. C* **2007**, *111*, 14849; c) X. Wu, P. L. Redmond, H. Liu, Y. Chen, M. Steigerwald, L. Brus, *J. Am. Chem. Soc.* **2008**, *130*, 9500; d) E. S. Thrall, A. Preska Steinberg, X. Wu, L. E. Brus, *J. Phys. Chem. C* **2013**, *117*, 26238.

[30] A. E. Schlather, A. Manjavacas, A. Lauchner, V. S. Marangoni, C. J. DeSantis, P. Nordlander, N. J. Halas, *J. Phys. Chem. Lett.* **2017**, *8*, 2060.

[31] P. Narang, R. Sundararaman, H. A. Atwater, *Nanophotonics* **2016**, *5*, 96.

[32] Z. Zhang, J. T. Yates, *Chem. Rev.* **2012**, *112*, 5520.

[33] a) J. E. Thorne, S. Li, C. Du, G. Qin, D. Wang, *J. Phys. Chem. Lett.* **2015**, *6*, 4083; b) Y. Kuang, T. Yamada, K. Domen, *Joule* **2017**, *1*, 290.

[34] C. Urso, M. Barawi, R. Gaspari, G. Sirigu, I. Kriegel, M. Zavelani-Rossi, F. Scotognella, M. Manca, M. Prato, L. De Trizio, L. Manna, *J. Am. Chem. Soc.* **2016**, *139*, 1198.

[35] A. Iqbal, K. H. Bevan, *J. Phys. Chem. C* **2018**, *122*, 30.

[36] W. S. Bourée, M. S. Prévot, X. A. Jeanbourquin, N. Guijarro, M. Johnson, F. L. Formal, K. Sivula, *Adv. Mater.* **2016**, *28*, 9308.

[37] a) K. Sivula, F. L.e Formal, M. Gratzel, *ChemSusChem* **2011**, *4*, 432; b) D. A. Wheeler, G. Wang, Y. Ling, Y. Li, J. Z. Zhang, *Energy Environ. Sci.* **2012**, *5*, 6682; c) Y. Lin, G. Yuan, S. Sheehan, S. Zhou, D. Wang, *Energy Environ. Sci.* **2011**, *4*, 4862; d) T. W. Hamann, *Dalton Trans.* **2012**, *41*, 7830; e) S. D. Tilley, M. Cornuz, K. Sivula, M. Gratzel, *Angew. Chem., Int. Ed.* **2010**, *49*, 6405.

[38] a) M. Xu, P. Da, H. Wu, D. Zhao, G. Zheng, *Nano Lett.* **2012**, *12*, 1503; b) G. Wang, X. Xiao, W. Li, Z. Lin, Z. Zhao, C. Chen, C. Wang, Y. Li, X. Huang, L. Miao, C. Jiang, Y. Huang, X. Duan, *Nano Lett.* **2015**, *15*, 4692.

[39] O. Diaz-Morales, F. Calle-Vallejo, C. de Munck, M. T. M. Koper, *Chem. Sci.* **2013**, *4*, 2334.

[40] E. Pensa, J. Gargiulo, A. Lauri, S. Schlücker, E. Cortés, S. A. Maier, *Nano Lett.* **2019**, *19*, 1867.

[41] F. Lin, S. W. Boettcher, *Nat. Mater.* **2014**, *13*, 81.

[42] Y. Yu, K. D. Wijesekara, X. Xi, K. A. Willets, *ACS Nano* **2019**, *13*, 3629.

[43] C. Zhan, B.-W. Liu, Y.-F. Huang, S. Hu, B. Ren, M. Moskovits, Z.-Q. Tian, *Nat. Commun.* **2019**, *10*, 2671.

[44] D. Klotz, D. S. Ellis, H. Dotan, A. Rothschild, *Phys. Chem. Chem. Phys.* **2016**, *18*, 23438.

[45] H. Zhu, H. Xie, Y. Yang, K. Wang, F. Zhao, W. Ye, W. Ni, *Nano Lett.* **2020**, *20*, 2423.

[46] a) W. Lu, N. Jiang, J. Wang, *Adv. Mater.* **2017**, *29*, 1604862; b) C. P. Byers, B. S. Hoener, W.-S. Chang, S. Link, C. F. Landes, *Nano Lett.* **2016**, *16*, 2314; c) C. P. Byers, H. Zhang, D. F. Swearer, M. Yorulmaz, B. S. Hoener, D. Huang, A. Hoggard, W.-S. Chang, P. Mulvaney, E. Ringe, N. J. Halas, P. Nordlander, S. Link, C. F. Landes, *Sci. Adv.* **2015**, *1*, 1500988; d) H. Nishi, T. Tatsuma, *Angew. Chem., Int. Ed.* **2016**, *55*, 10771; e) B. S. Hoener, H. Zhang, T. S. Heiderscheit, S. R. Kirchner, A. S. De Silva Indrasekara, R. Baiyasi, Y. Cai, P. Nordlander, S. Link, C. F. Landes, W.-S. Chang, *J. Phys. Chem. Lett.* **2017**, *8*, 2681.

**ADVANCED
SCIENCE NEWS**

www.advancedsciencenews.com

**ADVANCED
MATERIALS**

www.advmat.de

[47] V. Stockhausen, P. Martin, J. Ghilane, Y. Leroux, H. Randriamahazaka, J. Grand, N. Felidj, J. C. Lacroix, *J. Am. Chem. Soc.* **2010**, *132*, 10224.

[48] C. F. Bohren, *Am. J. Phys.* **1983**, *51*, 323.

[49] J. M. Luther, P. K. Jain, T. Ewers, A. P. Alivisatos, *Nat. Mater.* **2011**, *10*, 361.

[50] R. Alam, M. Labine, C. J. Karwacki, P. V. Kamat, *ACS Nano* **2016**, *10*, 2880.

[51] O. Zandi, A. Agrawal, A. B. Shearer, L. C. Reimnitz, C. J. Dahlman, C. M. Staller, D. J. Milliron, *Nat. Mater.* **2018**, *17*, 710.

[52] a) P. K. Jain, *J. Phys. Chem. C* **2019**, *123*, 24347; b) Y. Dubi, I. W. Un, Y. Sivan, *Chem. Sci.* **2020**, *11*, 5017.

Yuchao Zhang received his B.S. (2011) from Peking University and his Ph.D. (2016) under the supervision of Prof. Jincai Zhao and Prof. Chuncheng Chen at the Institute of Chemistry, Chinese Academy of Sciences. He then moved to the University of Florida and worked with Prof. Wei David Wei as a postdoctoral researcher (2016–2019). He has been a professor for physical chemistry at the Institute of Chemistry, Chinese Academy of Sciences since 2019. His research focuses on photoelectrochemistry on metal and semiconductor nanostructures and their photocatalytic applications in solar energy conversion.

Wei David is currently an associate professor in the Department of Chemistry of the University of Florida. He received his Ph.D. from the University of Texas at Austin with Mike White and trained as a postdoctoral researcher at Northwestern University with Chad Mirkin. His research interests are the novel electronic and optical properties of metallic and semiconductor nanomaterials and their applications in solar energy harvesting, conversion, and storage; visible-light photocatalysis; and chemical and biological detection.